Earth and Planetary Science Letters 391 (2014) 160–170

Contents lists available at ScienceDirect

Earth and Planetary Science Letters

www.elsevier.com/locate/epsl

Micro- and nanobands in late Archean and Palaeoproterozoic banded-iron formations as possible mineral records of annual and diurnal depositions

Yi-Liang Li *

Department of Earth Sciences, The University of Hong Kong, Pokfulam Road, Hong Kong

ARTICLE INFO

Article history:
Received 5 November 2013
Received in revised form 17 January 2014
Accepted 27 January 2014
Available online 19 February 2014
Editor: J. Lynch-Stieglitz

Keywords:
Precambrian
banded-iron formation
microbands
diurnal precipitation
annual depositions

ABSTRACT

The microbands in Precambrian banded-iron formations (BIFs) have been conjectured to record annual or even diurnal depositions. However, these bands have rarely been observed in high resolution at their true (micro) scale. Here, I suggest that nanobands of fine-grained hematite represent possible diurnal depositions and that microbands of chert/jasper represent possible annual depositions in three sets of BIFs: 2460-Myr BIFs from the Kuruman Iron Formation, Transvaal Supergroup of South Africa; 2480-Myr BIFs from the Dales Gorge Member of the Brockman Iron Formation, Western Australia; and 2728-Myr BIFs from the Hunter Mine Group, Abitibi Greenstone Belt, Canada. Observations made using scanning electron microscopy indicate that hematite and chert were syngenetic, and that there was a hiatus between their precipitation and the genesis of the remainder of the minerals containing structural Fe(II). Spindle-like grains of hematite, monocrystals of magnetite, and ferro-dolomite formed microbands of ~30–70 μm in thickness, which appear cyclically in the matrix of the chert. Neither the band-bound magnetite and dolomite nor the linear formations of the hematite spindles represent annual depositions due to their diagenetic features. The thinnest microbands (~3–~12 μm) were observed in the chert and jasper, and indicate depositional rates of 6.6–22.2 m/Myr in the BIFs. These rates are consistent with the integrated deposition rates calculated by geochronologic methods for the BIFs, if annual deposition is assumed. The ~26-nm nanobands observed only in hematite grains reflect an annual deposition of ~18.6 μm, or ~18.6 m/Myr, which is also consistent with the depositional rate calculated by geochronologic methods. It is tentatively suggested that these ~26-nm nanobands were formed from the diurnal precipitation of Fe(III) resulting from the circadian metabolism of Fe(II)-oxidizing or oxygen-evolving photosynthetic microorganisms, which slowed down the rise of atmospheric oxygen. The diurnal precipitation of Fe(III) as hematite and the annual deposition of silica as chert/jasper in the BIFs provide internal clocks that may facilitate the examination of short-term processes, such as ecological, oceanographic and climatic cycles, that are recorded by the mineral or chemical compositions of BIFs.

© 2014 The Author. Published by Elsevier B.V. Open access under CC BY-NC-ND license.

1. Introduction

Banded-iron formations (BIF) are the result of chemical depositions that occurred at one particular stage in Earth's evolution (3.8–1.8 Ga, Krapež et al., 2003; Klein, 2005), and are characterized by the dichotomous sedimentation of rough, silica-rich and iron-rich bands with hierarchical thicknesses and mineral structures. The fascinating question of how these bands were formed has received several highly controversial answers. Macrobands, mesobands and microbands are three distinct scales of bands recognized in BIFs, representing geological episodes with different time-scales and/or varying sedimentary rhythmites (Trendall and Blockley, 1970; Trendall, 2000). Mesobands contain microbands with a mean thickness of between 0.3 and 1.7 mm (e.g., Trendall, 2000); the thinnest microbands are ⩽0.05 mm thick (Morris, 1993; Williams, 2000), and were once thought to be the most informative bands (Morris, 1993). The thinnest microbands were envisaged as either diurnal precipitates (e.g., Cisne, 1984; Castro, 1994) or annual varves deposited as a result of seasonal oscillations in temperature and geochemistry (Trendall and Blockley, 1970; Trendall, 2000). Researchers have also suggested that these annual bandings

* Tel.: +852 28598021; fax: +852 25176912.
E-mail address: yiliang@hku.hk.

http://dx.doi.org/10.1016/j.epsl.2014.01.044
0012-821X © 2014 The Author. Published by Elsevier B.V. Open access under CC BY-NC-ND license.

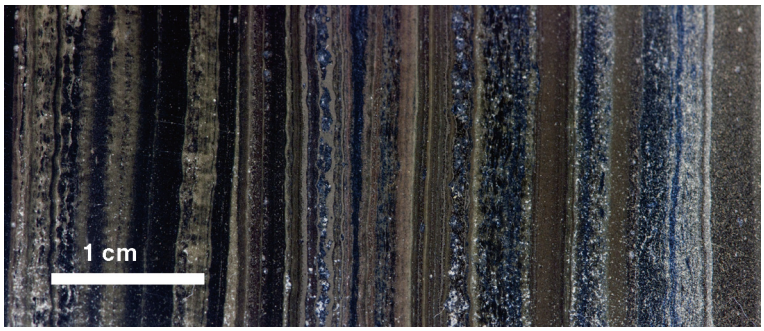

Fig. 1. Optical image of the segment of the Kuruman BIF sampled in this study.

reflect longer climatic cycles due to their cyclical appearance (see Walker and Zahnle, 1986 who proposed a 23.3-year cycle).

The deposition rates of BIFs can be determined by geochronologic methods only when they have been sandwiched by volcanic tuffaceous rocks containing minerals subject to radioactive dating. Using this method, the integrated depositional rates of BIFs have been calculated at time resolutions as high as ±3 Myr (e.g., Trendall, 2000, 2002; Pickard, 2002, 2003; Trendall et al., 2004). However, no intrinsic speedometry with a time scale comparable to that of climatic and ecological cycles can be used to evaluate ocean-deposited banded iron. Although such bands, especially the famous "Trendall bands" of the Dales Gorge in Western Australia (e.g., Morris, 1993) and the Kuruman Iron Formation of South Africa, have well-developed rhythmites comparable to those of post-Cambrian deposits, the lack of accurate estimates of depositional rates makes it difficult to reconstruct the climatic, oceanographic and ecological cycles involved.

Baur et al. (1985) measured the carbon- and oxygen-isotopic compositions of a set of 32 adjacent microbands at millimeter scale, and found rough variations between adjacent bands. Recent geochemical studies of BIFs have revealed extensive interactions between the ocean, the atmosphere and their complementary biospheres, including a slowing down of the rise in atmospheric oxygen (e.g., Anbar and Knoll, 2002; Bjerrum and Canfield, 2002; Kump and Barley, 2007; Frei et al., 2009; Fru et al., 2013; Konhauser et al., 2009, 2011; Poulton et al., 2004). In particular, studies involving *in situ* measurements of unconventional isotopes in BIFs have great potential to illuminate the processes related to ocean chemistry, (bio)mineralization and diagenesis (e.g., Frost et al., 2007; Marin-Carbonne et al., 2011; Steinhoefel et al., 2009, 2010). The degree of accuracy of these analyses relies heavily on the microlandscapes of the BIFs under study. First, the geochemical behavior of trace elements or unconventional isotopes in BIFs is determined by their partitioning among submicrometer- or even nanometer-scale minerals; second, the size and distribution of magnetite crystals in BIFs may directly influence the distribution of electron beams and magnetic fields during *in situ* analysis. However, only a few high-resolution petrologic and mineralogical studies of BIFs have been carried out using electron microscopes (e.g., Ahn and Buseck, 1990; Kolo et al., 2009; Li et al., 2011, 2013a, 2013c; Huberty et al., 2012). In this study, electron microscopes are used to characterize BIF minerals from the early Palaeoproterozoic and late Archean eras, with initial attentions to micro- and nanobands in BIF hematite grains. Explanations of chert/jasper bands as the result of annual deposition and hematite nanobands as the result of diurnal precipitation are found to be consistent with the depositional rates of BIFs previously determined by geochronologic methods.

2. Samples and methods

Representative BIF samples from the late Archaen and early Palaeoproterozoic eras were examined. The BIFs sampled from the Kuruman Formation and Dales Gorge are of a similar age, and researchers have suggested that they formed on the same continent (Pickard 2002, 2003; Beukes and Gutzmer, 2008). The Kuruman Iron Formation is in the Transvaal Supergroup of the Northern Cape Province, South Africa; it has a SHRIMP U–Pb age of 2460 Myr (Pickard, 2003), and its peak metamorphic temperature has never exceeded 110–170 °C (Miyano and Beukes, 1984). The Dales Gorge Member BIF is in the Brockman Supersequence of the Hamersley Range Megasequence. It is 2480 Myr old (Pickard, 2002), and is known to have experienced low-grade metamorphism at 60–160 °C (Kaufman et al., 1990). The Dales Gorge Members are made of alternating layers of fine-grained iron oxides and chert, with occasional thin layers of carbonate (Ewers and Morris, 1981; Dukino et al., 2000). The Abitibi BIF is embedded in the uppermost section of the Hunter Mine Group, a bimodal volcanic complex in the Abitibi Greenstone Belt, and is 2728 Myr old (Mueller and Mortensen, 2002). The sample for this study was taken from the chert–jasper–magnetite facies preserved in a large, folded rip-up clast within volcanic breccias (Chown et al., 2000; Weiershäuser and Spooner, 2005). Fig. 1 shows part of the banding structures of a hand specimen from the Kuruman Iron Formation, in which more than 100 microbands can be identified easily using the naked eye. As emphasis is placed in this report on the general features of microbands in BIFs, the sources of the samples are not specified, unless otherwise noted.

A Hitachi S-4800 FEG scanning electron microscope (SEM) was used in the secondary-electron (SE) mode at a low voltage (3–5 kV) to characterize the surface structures. The same microscope was used in the backscatter-electron (BSE) mode at a high voltage (20 kV) to portray electron density, which results in textural differentiation. In terms of structural differentiation, a Tecnai G2 20 S-TWIN transmission electron microscope (STEM) was used to characterize the size and morphological behavior of single crystals of ultrafine hematite, and equipped energy-dispersive X-ray spectroscopy (EDS) was used to measure the chemical compositions.

3. Results

Consistent with previous petrologic observations (Trendall and Blockley, 1970; Morris, 1993; Trendall, 2002; Krapež et al., 2003), the SEM observations showed bands of various thicknesses, from macro scale (>cm, Fig. 1) to just a few μm. Hereafter, the term "microband" is used to describe bands with truly μm-scale thicknesses. Such microbands may be made of chert/jasper, magnetite, ferro-dolomite, hematite grains or stilpnomelane (Stp). Although

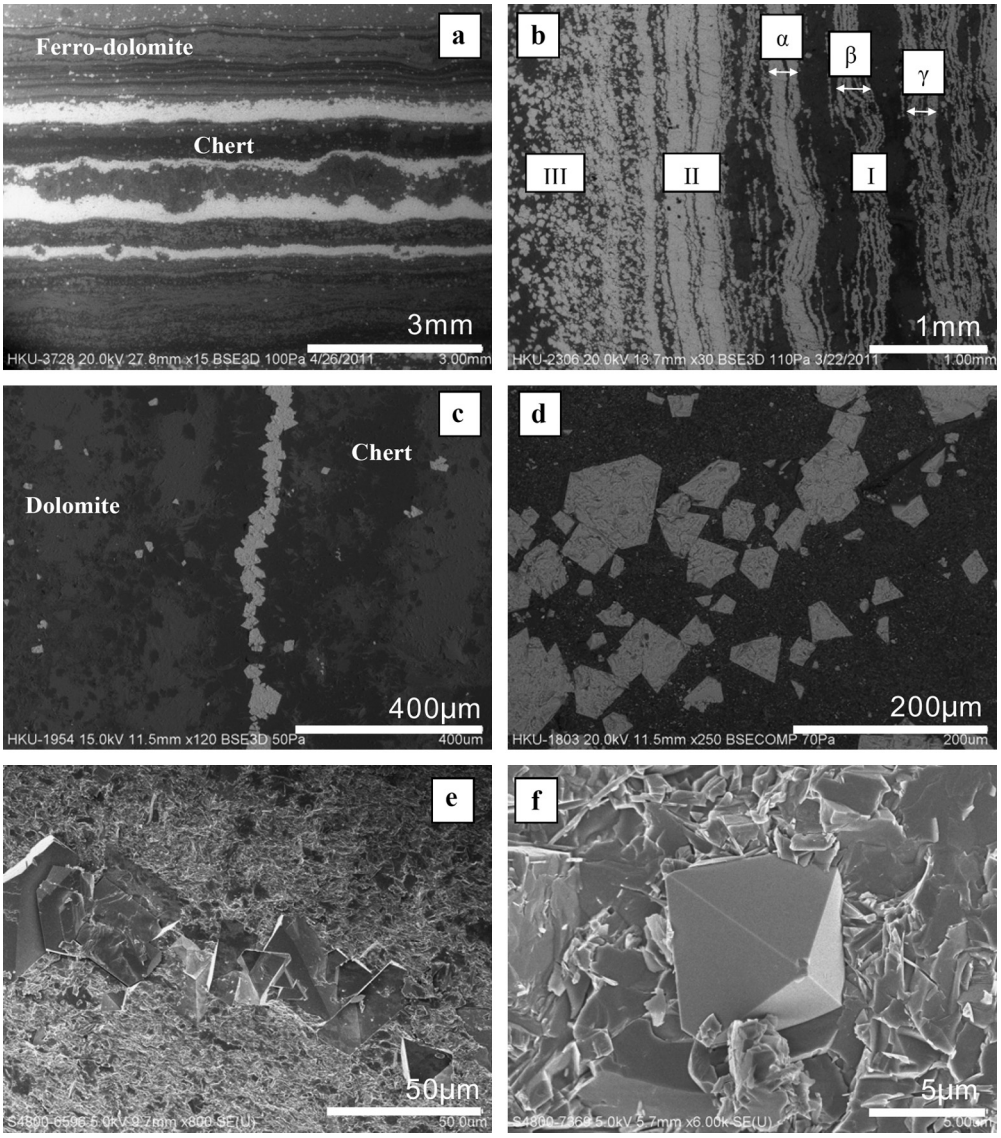

Fig. 2. Microbands of magnetite. The micrographs (a)–(d) are BSE-mode images on polished surfaces, while (e)–(f) are SE-mode images on unpolished surfaces. In (a) and (b), the brightest bands are magnetite and the darkest bands are chert. The grey bands in (a) are a combination of hematite, ferro-carbonate and stilpnomelane. (c) is a microband made of lined-up single crystals of magnetite. (d) shows euhedral magnetite crystals of a wide range of sizes in the matrix of chert. (e) is a microband of magnetite in the jasperous matrix. (f) is a euhedral magnetite crystal in the jasperous matrix without magnetite-rich bands nearby.

the thinnest microbands varied in thickness according to the nature/diagenesis of the minerals involved, all of the microbands had clear rather than diffuse boundaries, with the exception of the Stp microbands.

3.1. Magnetite microbands

The brightest bands and scattered single crystals shown in Figs. 2a and 2b, which represent BSE mode observations, were of magnetite. Single magnetite crystals ranging from ~5 to nearly 100 μm in size formed broad, visually observable magnetite-rich bands (Fig. 2a). Microbands made of clusters of single magnetite crystals (type I in Fig. 2b), ~200-μm bands of tightly aggregated magnetite (type II in Fig. 2b), and disseminated magnetite (type III in Fig. 2b) were observed in both the Kuruman BIF sample and the Dales Gorge BIF sample. The thinnest magnetite bands were made of lined-up single crystals of magnetite with an average size of around 33 μm (Figs. 2b and 2c). For comparison, Fig. 2d shows magnetite crystals with a large size distribution (~5 to ~100 μm) disseminated in a matrix of chert. Fig. 2e shows lined-up magnetite crystals observed in the SE mode, and Fig. 2f displays a single magnetite crystal coexisting with hematite grains.

3.2. Ferro-dolomite microbands

Ferro-dolomite macrobands were observed in areas with high density of ferro-dolomite microbands in the chert matrix (Fig. 2a, Figs. 3a and 3b), but no pure macro-scale dolomite bands were found in the samples. Microbands of dolomite with thicknesses ranging from ~23 μm to ~50 μm were found to be common in the dolomite-rich layers (Figs. 3a and 3c). In particular, Fig. 3c shows a truncated dolomite microband against a chert and hematite background, indicating its later formation. No microbands of siderite were observed, but siderite relics were found in the dolomite microbands (Fig. 3d). As siderite can be directly precipitated from anoxic, Fe(II)-saturated and bicarbonate-saturated pore water in marine sediments (e.g., Morris, 1993; Beukes and Gutzmer, 2008),

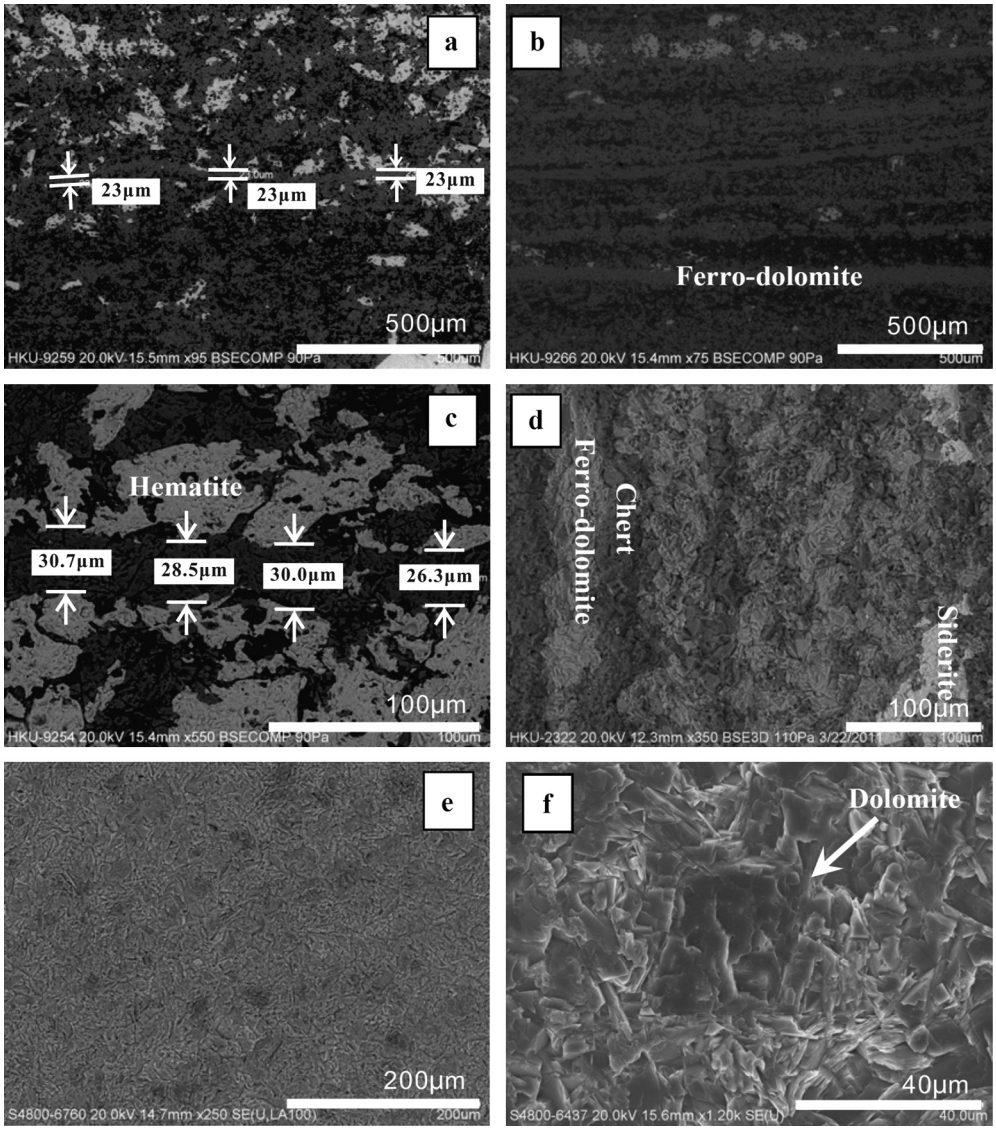

Fig. 3. Microbands of ferro-dolomite. In (a), a dolomite microband of ~23 μm is visible at the center of the image. (b) shows the cyclical appearance of dolomite microbands of similar thicknesses in the matrix of chert. (c) shows a dolomite microband cutting through hematite grains with chert as the earliest mineral composed in the structure. (d) shows the alternative chert and ferro-dolomite microbands and siderite relics. The darker dots in (e) are scattered dolomite crystals in the matrix of jasperous material observed in the BSE mode. (f) shows the single dolomite crystal in (e) observed in the SE mode.

the replacement of siderite with ferro-dolomite may have occurred during the diagenetic stage, similar to the widely observed replacement of Ca-carbonate by dolomite (e.g., Eriksson et al., 1975). The dissemination of dolomite was also observed in the matrix of the chert, which contained euhedral crystals of 10 to >50 μm in length. The dark spots in Fig. 3e are dolomite crystals viewed in the BSE mode, one of which appears at the center of Fig. 3f was observed at a low voltage in the SE mode.

3.3. Stilpnomelane microbands

In the samples under study, no thick bands of stilpnomelane (Stp) were observed. Instead, Stp crystals in Stp-lutite had made bands of ~200 μm to >400 μm, which showed diffuse features (Figs. 4a and 4b). The Stp bands shown in Fig. 4a were found in the magnetite- and carbonate-containing chert matrix, and the Stp-bands and magnetite bands shown in Fig. 4b were found in the dolomitic matrix. Fig. 4c represents the amplification of the Stp distributed in the carbonate-rich areas of the chert matrix (depicted in grey), and Fig. 4d shows, in particular, bundles of Stp forming wall rock of magnetite. The paucity of Stp, together with the previously reported appearance of quartz nanocrystals in typical BIFs (Li et al., 2013a), indicates the diagenesis of episodically rained aeolian fine particles from distal subaerial volcanic activity (Kump and Barley, 2007).

3.4. Chert microbands

The chert and jasper microbands were much thinner than the thinnest microbands of magnetite and dolomite or the bands made of spindle-like hematite grains. Figs. 5a and 5b show chert and jasper bands on the polished surfaces of the samples, observed in the BSE mode. Fig. 5a shows chert bands (dark) in the dolomite matrix, which were traced to >1 cm along their strikes using SEM, providing evidence of their genuine sedimentary genesis. Fig. 5b shows alternating chert microbands (dark) and jasper bands (grey). Figs. 5c and 5d show chert microbands (dark bands marked for thickness) as narrow as 2.7–10.2 μm on freshly uncovered surfaces, observed in the SE mode. Alternating jasper–chert–jasper bands (11.5–11.5–6.2 μm) are shown at the center of Fig. 5e, and

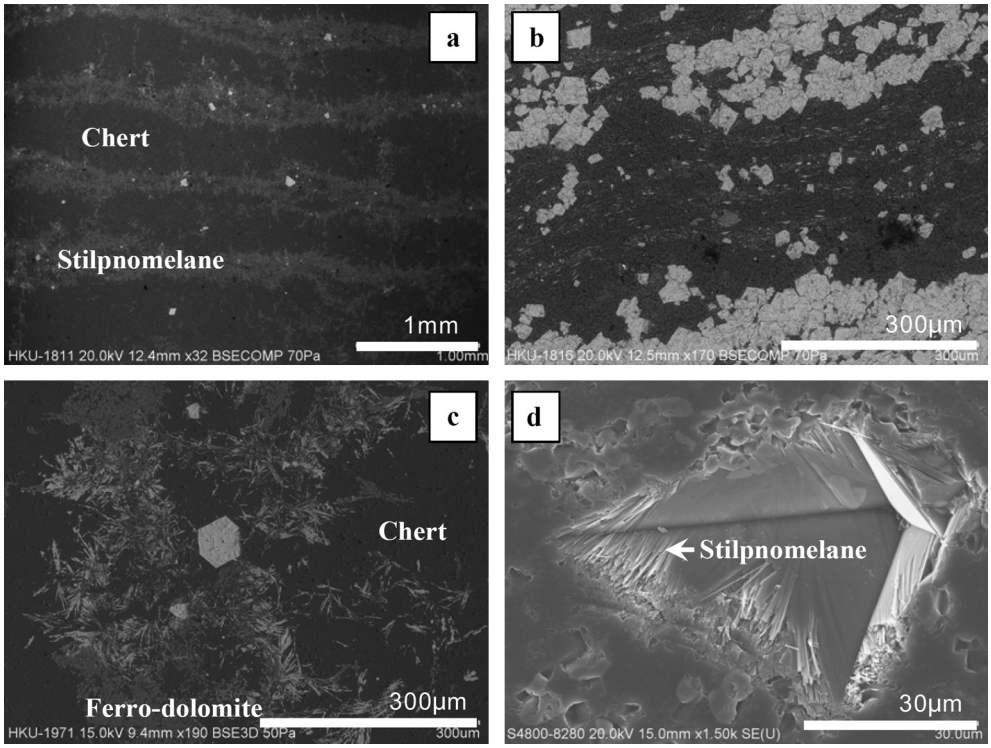

Fig. 4. Stilpnomelane microbands and their petrologic appearance. (a) shows the periodic appearance of stilpnomelane microbands of a few hundred μm in the matrix of chert. (b) shows the periodic appearance of ~50-μm microbands rich in stilpnomelane in the matrix of dolomite. (c) shows stilpnomelane bundles, dolomite and magnetite in the matrix of chert. In (d), the falling-off of a magnetite crystal reveals bundles of stilpnomelane.

a single jasper microband (14.8 μm) appears in the upper part of the micrograph. Fig. 5f shows the further amplification of the area highlighted in Fig. 5e. The dissemination of the magnetite crystals again indicates their crystallization after the formation of the chert, jasper and dolomite bands (Figs. 5e and 5f).

3.5. Microbands made of spindle-like hematite grains

SEM revealed the hematite microbands to be made of grains, rather than continuous lamina. These grains were of two types: irregular grains with sizes ranging from a few tens of μm to a few hundred μm (Li et al., 2013a), and spindle-like particles sized between a few μm and ~10 μm. Hematite spindles of a few μm in size had lined up to make microbands of around 70 μm (Fig. 6a) in the dolomitic matrix. These microbands appeared periodically in the chert matrix along with hematite spindles of approximately the same size but a lower density, scattered between two bands (Fig. 6b). In addition to the hematite spindles and the dolomite (grey), scattered chert (the darkest dots) could still be observed, which was probably the earliest precipitated mineral (Fig. 6c). Figs. 6c and 6d show that the hematite band and the scattered spindles were both a few μm to >10 μm in size. Fig. 6e shows hematite spindles of a few tens of μm in size, and the cycles highlight the chert relics in the hematite spindles. Fig. 6f shows a particular >20-μm hematite spindle.

3.6. Hematite nanobands

In addition to a trace amount of nano-apatite reported previously (Li et al., 2011), the minerals hematite and chert, which are abundant in BIFs, were found to exhibit either nano-crystal dimensions or amorphous features (Li et al., 2013a). At the μm scale, the hematite appeared as grains as large as >100 μm or aggregated spindles, as described (Fig. 6). When observed at much high spatial resolution, the newly uncovered surfaces of the hematite grains in the BIFs showed rare wavy laminates at the nanometer scale (Fig. 7a), which appeared as contoured structures when observed on the surfaces at different angles (Figs. 7b and 7c). Fig. 7d shows the horizontally contoured structure of the thin hematite laminates, the thickness of which was measured at 26 nm. Fig. 7e and Fig. 7f (upper-left corner) represent the contoured structures of ultra-thin banding structures in the hematite grains. The layers shown in Figs. 7e and 7f were between 17 and 26 nm in thickness, with an average thickness of 21 nm. No hierarchical bands were observed between these nanometer structures and the micrometer laminates of chert or jasper, the thinnest microbands.

The hematite matrix showed better-preserved nanobanding structures in the pits formed after the magnetite crystals (Figs. 8a–8c). These structures were observed in the BIFs from the Dales Gorge (not shown), the Kuruman Formation (e.g., Figs. 8a and 8b) and the Abitibi Greenstone Belt (e.g., Fig. 8c). Detailed characterizations are presented in Fig. 9. Fig. 9a displays a hematite grain with a pit after a cluster of magnetite crystals, showing ultrafine horizontal structures of hematite. Figs. 9b and 9c are further amplifications of the highlighted areas in Fig. 9a. Figs. 9d and 9f represent step-by-step amplifications of the zoning structure shown in Fig. 9c. The average thickness of the fine lamina can be easily calculated at 26 nm from Figs. 9e and 9f: a result similar to those of calculations based on the nanobands, as shown in Fig. 7. If this thickness is assumed to reflect the daily precipitation of hematite, that is, 26 nm/day, it is equivalent to the oxidation of Fe(II) at 17 μM/day m^2 or the deposition of Fe_2O_3 (hematite) at a rate of 1 g/yr m^2 from the euphotic zone of the water column.

4. Discussion

The aforementioned observations can be summarized as follows: (1) All of the major BIF minerals—chert, magnetite, hematite, ferro-dolomite and Stp—are capable of forming microbands from a

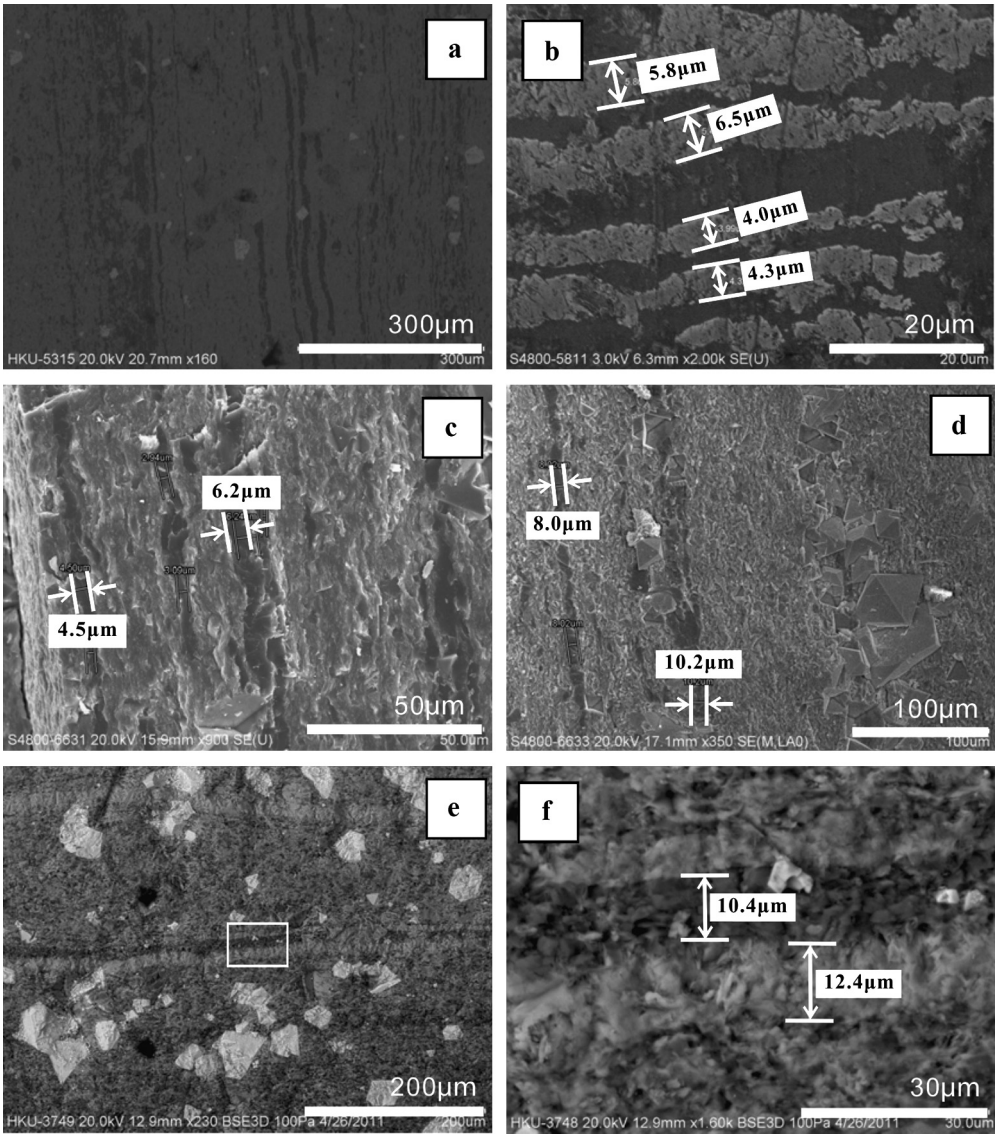

Fig. 5. Microbands of silica and jasper. In (a), chert microbands of <10 μm (dark) in a jasperous matrix are observed on a polished surface. (b) and (c) show <6-μm chert microbands in the matrix of jasper. (d) shows chert and magnetite microbands in the jasperous matrix. In (e), chert (black bands), jasper bands (grey) and desiminated magnetite crystals appear in the matrix of chert and jasper. (f) highlights the amplification of the chert and jasper microbands shows in (e).

few μm to about 100 μm in thickness. In particular, the hematite microbands were found to be made of μm-sized spindle-like grains. (2) The thinnest microbands were made of chert/jasper. (3) The much thinner nanobands of ~26 nm were only observed in hematite grains. Magnetite, dolomite and Stp were found either in the form of microbands or as disseminated minerals randomly distributed in the matrix (e.g., magnetite, Li et al., 2013b). The observation that Stp was recrystallized from clay minerals in the tuffaceous-rich layers (Pickard, 2002, 2003; Trendall et al., 2004) is consistent with the diagenetic features of Stp (Fig. 2d, Fig. 3e, Fig. 4c, Fig. 5e).

4.1. Hematite nanobands as the result of the diurnal precipitation of Fe(III) by the circadian metabolism of Fe(II)-oxidizing bacteria or O_2-producing phototrophs

Hematite was the only mineral found in these BIFs, with an ultrafine crystal size of 3–5 nm (Ahn and Buseck, 1990; Li et al., 2013a). The ultrafine contours and horizontal structures formed by these hematite crystals (Fig. 7) are petrologic structures that differ from the layer-growth topographic structures observed on >10-μm hematite monocrystals (Rosso et al., 2003). The "primary" hematite crystals, measured at about 3–5 nm (Ahn and Buseck, 1990; Li et al., 2013a), were of a very similar size to ferrihydrite synthesized at room temperature (~2 nm, Liu et al., 2005; Posth et al., 2013), which suggests that a solid-state transformation took place in a short time without altering the petrologic microstructure. The frequent appearance of hematite as grains of a few tens of μm to >100 μm in size indicates that its original sedimentary structure was fragile, and was destroyed during the later crystallization of authigenic, Fe^{2+}-containing, μm-scale minerals. It was subsequently characterized by an ongoing increase in crystal size (Li et al., 2013b).

If the hematite nanobands (Figs. 7–9) are assumed to represent diurnal precipitation (26 nm per day), the rate of hematite deposition in the BIFs can easily be calculated as 18.6 μm per annum. This is equivalent to 18.6 m/Myr if one year 2.5 Gyr ago had 714 days (Arbab, 2009; Costas et al., 1996), or 13.4 μm if one year had 514 days (Walker and Zahnle, 1986) in the period from the late Archean to the early Palaeoproterozoic eras. The thinnest

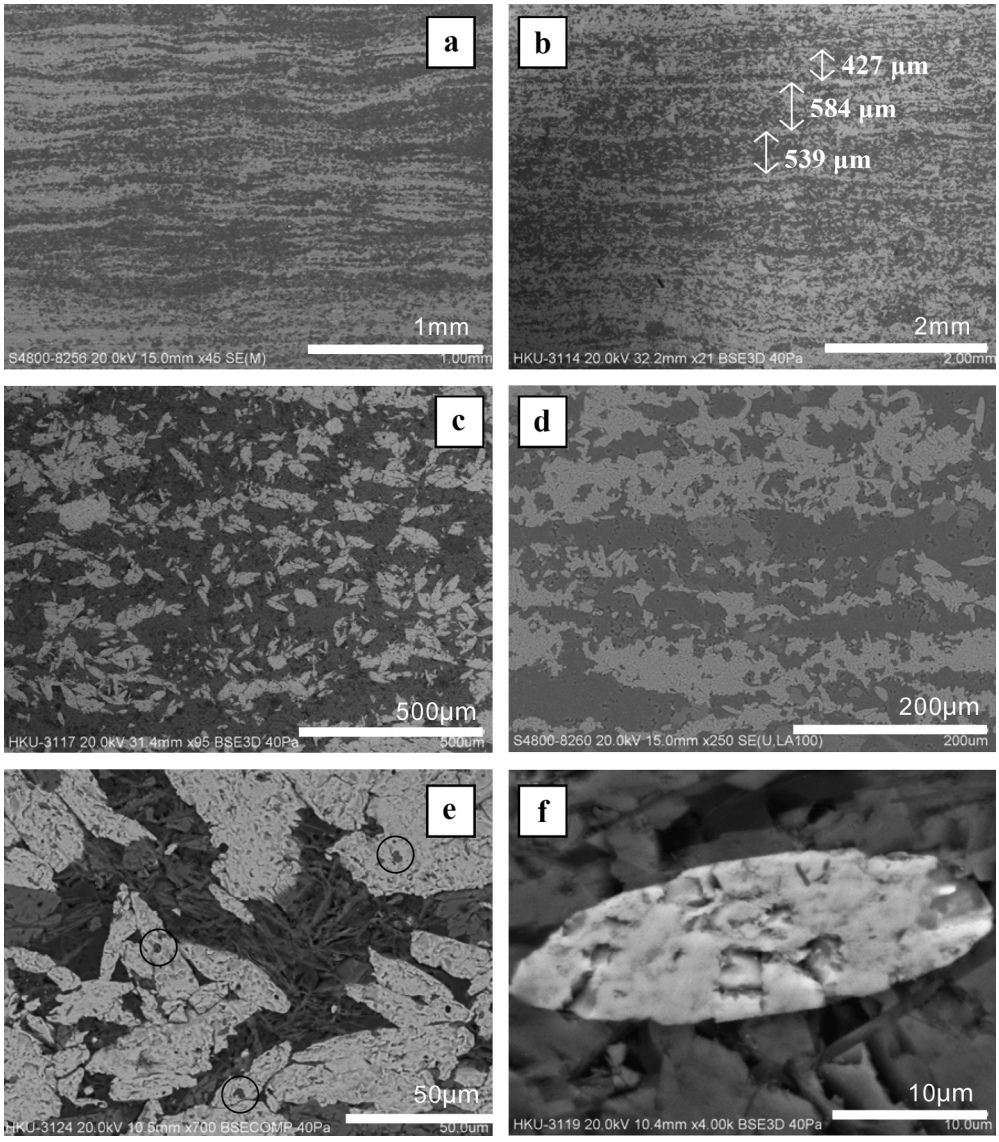

Fig. 6. Microbands of hematite. (a) shows microbands of hematite with thicknesses ranging between 30 and ~100 µm. (b) shows the periodic appearance of hematite microbands of 45–90 µm in a hematite-rich chert matrix. (c) shows spindle-shaped hematite grains mixed with ferro-dolomite (grey) and chert (dark). In (d), bands with a high concentration of hematite spindles are visible in a matrix of ferro-dolomite and chert. (e) shows the coexistence of the spindle-formed hematite grains with carbonate and stilpnomelane. The cyclical dark spots on the spindles of hematite are globules of chert. (f) represents a particularly large hematite spindle.

microbands observed in the chert/jasper were >100 times thicker than the hematite nanobands, and no banding structures with thickness were found between the nanobands of hematite and the microbands of jasper or chert. If the microbands of chert/jasper represent annual depositions, it is reasonable to interpret the nanobands as the result of diurnal precipitation.

As the Fe(III) precursor of hematite in the sampled BIFs was precipitated in seawater below the tidal wave (Morris, 1993; Walter and Hofmann, 1983; Beukes and Gutzmer, 2008), these nano-scale layers differ from the submicrometer-scale bands of tidal rhythmites observed in the 2450-Myr BIF from the Weeli Wolli Formation, Western Australia (Williams, 2000). The ultrafine oxyhydroxide (e.g., ferrihydrite) particles were precipitated in the euphotic zone (Kappler et al., 2005) and gradually deposited at the bottom of the ocean, where the water was not disturbed by microbial activity or waves (e.g., Walter and Hofmann, 1983). SEM observations showing the lack of banding structures with thickness between the chert/jasper microbands and the hematite nanobands indicate the absence of monthly cyclicity.

The diurnal deposition of ferric iron is consistent with the emergence of circadian metabolism of photosynthetic microorganisms in the Archean–Palaeoproterozoic oceans (Dvornyk et al., 2003; Golden and Canales, 2003). It is suggested that the phototrophic microorganisms oxidized the dissolved Fe(II) either by enzymatic Fe(II)-metabolism or indirectly by biogenic O_2, which led to the deposition of the Fe(III) precursor of hematite in the BIFs (Brocks et al., 1999; Konhauser et al., 2002, 2009; Kappler et al., 2005; Kump and Barley, 2007; Posth et al., 2008). The ecophysiology of modern microbial photoautotrophs is similar to that of their ancient ancestors (e.g., Sergeev et al., 2002; Saito et al., 2003). Covarying temperature and irradiance periods (Berman-Frank et al., 2001) can result in rhythmic sedimentary structures representing diurnal, seasonal or longer time-scales in biomats (Epping and Kühl, 2000; Stal and Krumbein, 1986). The Fe(II) oxidizer may have been a photoautotroph (Kappler et al., 2005) whose physiological and metabolic habits were synchronized with the alternation between light and dark (Golden and Canales, 2003). Although temperature periodicity was found to exhibit the same light–dark

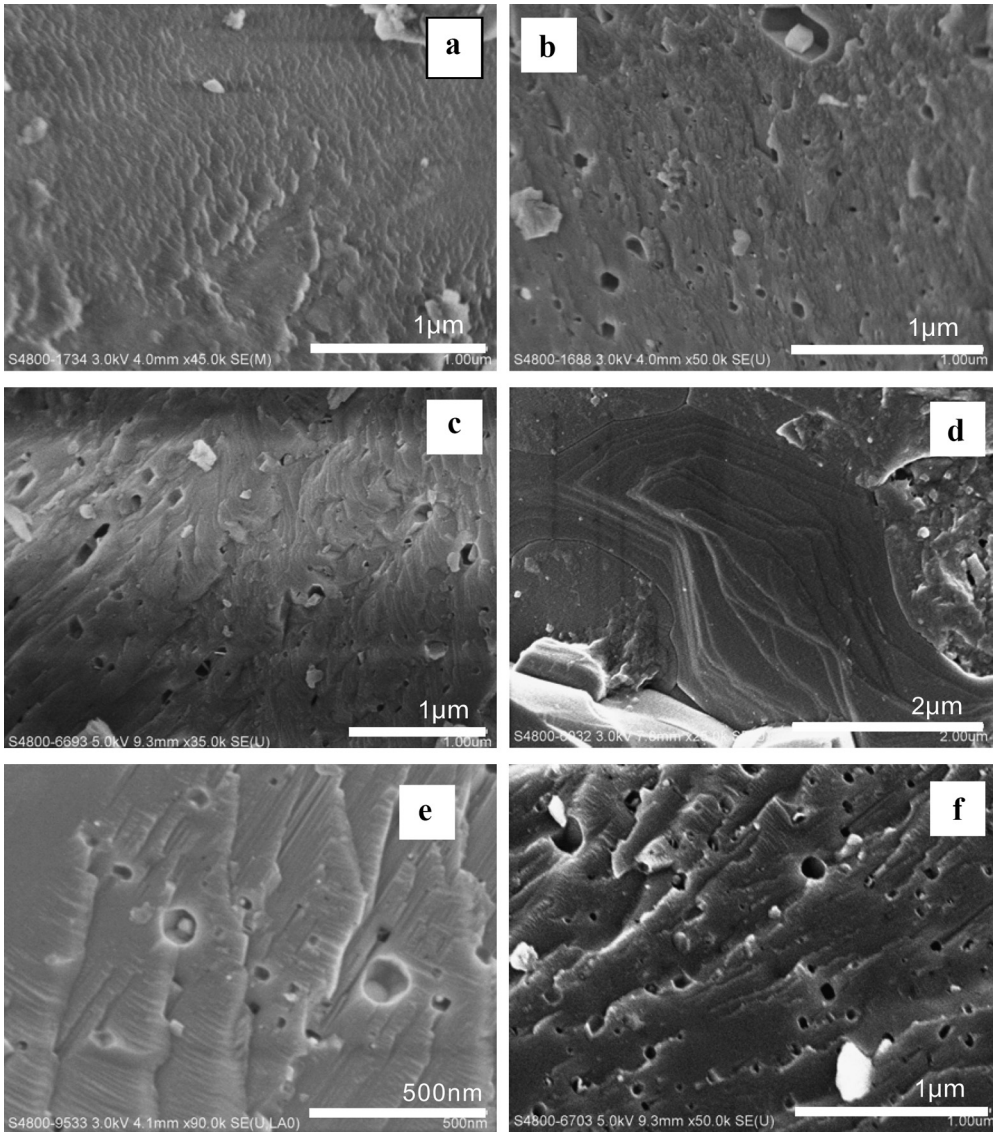

Fig. 7. Structure of hematite grains. (a) shows the wavy structure of hematite at the nano scale. (b) shows erosional features with a quartz nanocrystal and pits on the surface. (c) represents nano-scale laminated hematite. (d) shows the horizontally contoured structure of the hematite. (e) and (f) show horizontally contoured structures in the grains of hematite.

alternation, the daily precipitation of ferric oxyhydroxide did not result from the temperature dependency of phototrophic Fe(II) oxidization (e.g., Hegler et al., 2008; Posth et al., 2008), but from synchronized diurnal metabolism. In seawater with banded-iron deposits, the circadian metabolism of photosynthetic microorganisms such as cyanobacteria only produced O_2 during the day-time (e.g., Stal and Krumbein, 1986; Golden and Canales, 2003), which in turn oxidized soluble Fe(II) to ferric oxyhydroxide in the euphotic zone. This combination of geochemical and biological processes may have produced layers of Fe(III) oxides with sufficient contrast via synchronized energy, physiological, chemical, and biomineralization oscillations. The daily precipitated Fe(III) (e.g., ferrihydrite) could eventually have been transformed into hematite nano-films without destroying the banding structure via a solid-state transformation mechanism, as demonstrated chemically (Liu et al., 2005). The formation of these nanobands of hematite, and the fact that hematite was not observed mixing with Fe(II) minerals (Fig. 7), imply that Fe(II) was biologically oxidized at a sufficiently high efficiency (e.g., Hallberg and Ferris, 2004), even with an increased supply of Fe(II) to the oceans (e.g., Barley et al., 1997), to prevent the precipitation of Fe(II) minerals (Konhauser et al., 2007). Although the photochemical oxidation of Fe(II) (Braterman et al., 1983) is also synchronized with light–dark alternation, its oxidation rate is insufficient to account for the deposition of massive iron bands in the sampled BIFs (e.g., Kappler et al., 2005; Konhauser et al., 2007).

4.2. The thinnest chert microbands as the result of annual precipitation directly from the ocean

Assuming that the ~2.7–10-μm chert bands resulted from annual deposition, the deposition of silica in the range of 2.7–10.2 m per Ma, is consistent with the integrated depositional rates previously calculated by detailed dating of the BIFs from the Dales Gorge Member of Australia and the Kuruman Formation of South Africa (Pickard, 2003; Trendall et al., 2004). As chert and jasper are both siliceous materials that form alternating bands (Figs. 5c and 5e), their continuous precipitation may be the result of seasonal changes in physicochemistry (Wang et al., 2009) or biological activity. The observations made during this study indicate that only

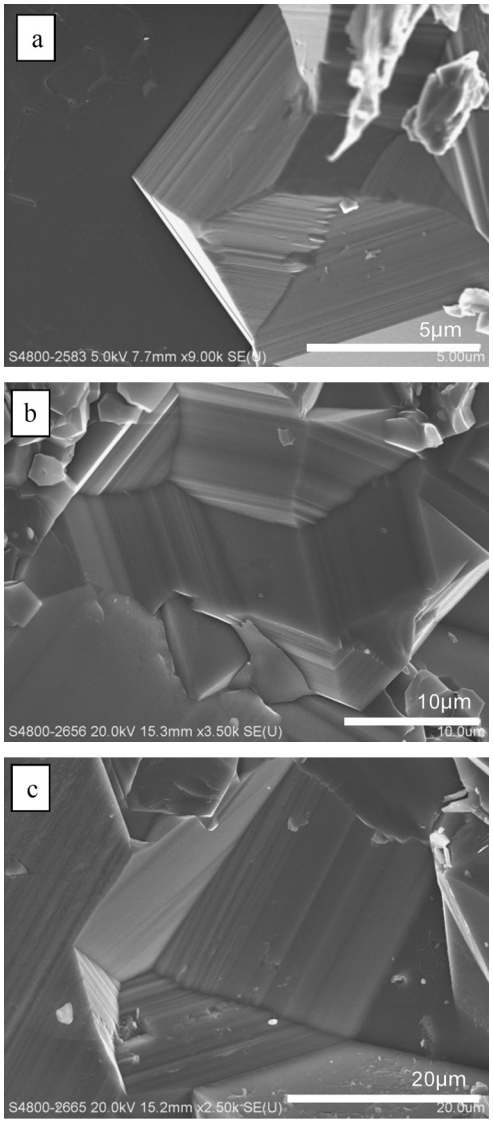

Fig. 8. A collection of three pits after the falling-off of magnetite crystals, all showing ultrafine horizontal structures.

hematite nanobands and chert/jasper microbands are significant to the evaluation of depositional rates according to band thickness. The annual deposition rates calculated in this study are in the same range as the depositional rates estimated for the Weeli Wolli BIF (Trendall, 2002) and the Dales Gorge BIF (Trendall, 2000) by radioactive chronologic dating. If the annual deposition of iron as hematite was 18.6 μm and the annual precipitation of silica as chert was ∼10 μm, and these two minerals represent the earliest precipitations in banded iron, then the thinnest visual microbands in silica- and iron-rich bands represent ∼30 years deposition, which is consistent with previous observations (Walker and Zahnle, 1986).

4.3. Microbands of dolomite, magnetite and Stp carry more diagenetic or low-grade metamorphic information

Disseminated magnetite was found to be scattered in many parts of the sampled BIFs (Fig. 2a, Fig. 4a, Fig. 5a, Fig. 8). The vertical transportation of iron-containing fluids may explain the continuing growth of magnetite (Frost et al., 2007; Pecoits et al., 2009). Li et al. (2013b) experimentally demonstrated that the magnetite produced during heterotrophic Fe(III) reduction can indeed grow bigger under low-grade metamorphic conditions when both active Fe(II) and Fe(III) are available. Posth et al. (2013) demonstrated the formation of both siderite and magnetite from reactions between ferrihydrite and glucose under metamorphic conditions similar to those of the BIFs from the Kuruman Iron Formation and Dales Gorge. In addition to the ferro-dolomite and magnetite microbands, disseminated ferro-dolomite and magnetite crystals of a wide range of sizes were found in the siliceous matrix (Fig. 2d and Fig. 3e). Their continuing growth is indicated by the activity of the Ostwald coarsening mechanism (e.g., Li et al., 2013b). These properties suggest that the microbands of magnetite or ferro-dolomite that continued to grow during diagenetic or low-grade metamorphic periods (e.g., Klein, 1973; Morris, 1980; Li et al., 2013b) were not the result of annual depositions. The coexistence of ferro-dolomite bands and relics of siderite offer evidence for the introduction of Ca^{2+} and Mg^{2+} by diagenetic/metamorphic fluids to the original minerals.

Although the hematite crystals in the samples were much smaller than the crystals of magnetite or dolomite (Ahn and Buseck, 1990; Li et al., 2013c), the spindle-like hematite grains bearing hematite microbands (Figs. 6c, 6e) were almost the same size as the monocrystals of magnetite and dolomite. Although the mechanism by which hematite spindles form is still unknown, the spindle-made microbands may have been syngenetic with the diagenetic growth of the magnetite or dolomite microbands. The straight lines of dolomite intersecting the hematite and chert in Fig. 3c indicate that the dolomite formed after the hematite and the chert. Similarly, the disseminating features (Figs. 2b and 2d) reveal that the magnetite microbands were the result of the continued growth of magnetite crystals under later diagenetic or low-grade metamorphic conditions (Li et al., 2013b). The appearance of a single microband of magnetite made of magnetite monocrystals in a much wider band of chert and dolomite (Fig. 2c) excluded the possibility of annual deposition, although the mechanisms by which these microbands form are still unclear. The dolomite monocrystals disseminated in the chert matrix are approximately the same size (∼20 μm) as the magnetite monocrystals, suggesting that the dolomite microbands are similar to the magnetite single-crystal bands (Fig. 3e).

5. Conclusions

Nanobands of 17–26 nm in hematite grains and microbands formed from dolomite, magnetite and spindle-like hematite grains with thicknesses between 20 and >50 μm were observed in BIFs from the late Archean and Palaeoproterozoic eras. The thinnest microbands (2.7–12.2 μm) were found in chert/jasper. The results suggest that the hematite nanobands represent the diurnal precipitation of Fe(III) resulting from the circadian metabolism of Fe(II) or oxidation by the biogenic O_2 produced by photoautotrophic bacteria. The diurnal precipitation of hematite at 17–26 nm and the annual deposition of chert/jasper microbands are consistent with the depositional rates of BIFs previously determined by high-resolution geochronologic methods. The formation of the microbands of magnetite, dolomite and Stilpnomelane, and perhaps also the spindle-like hematite grains, were syngenetic, and were influenced by the band-bound continuing growth of the respective crystals during diagenetic or low-grade metamorphism. The observations made in this study of the daily and annual deposition rhythms of minerals in banded-iron formations provide internal temporal measurements that will facilitate future studies of the short-time-scale cyclicities of the ecological, oceanographic and climatic processes reflected in mineral and chemical compositions.

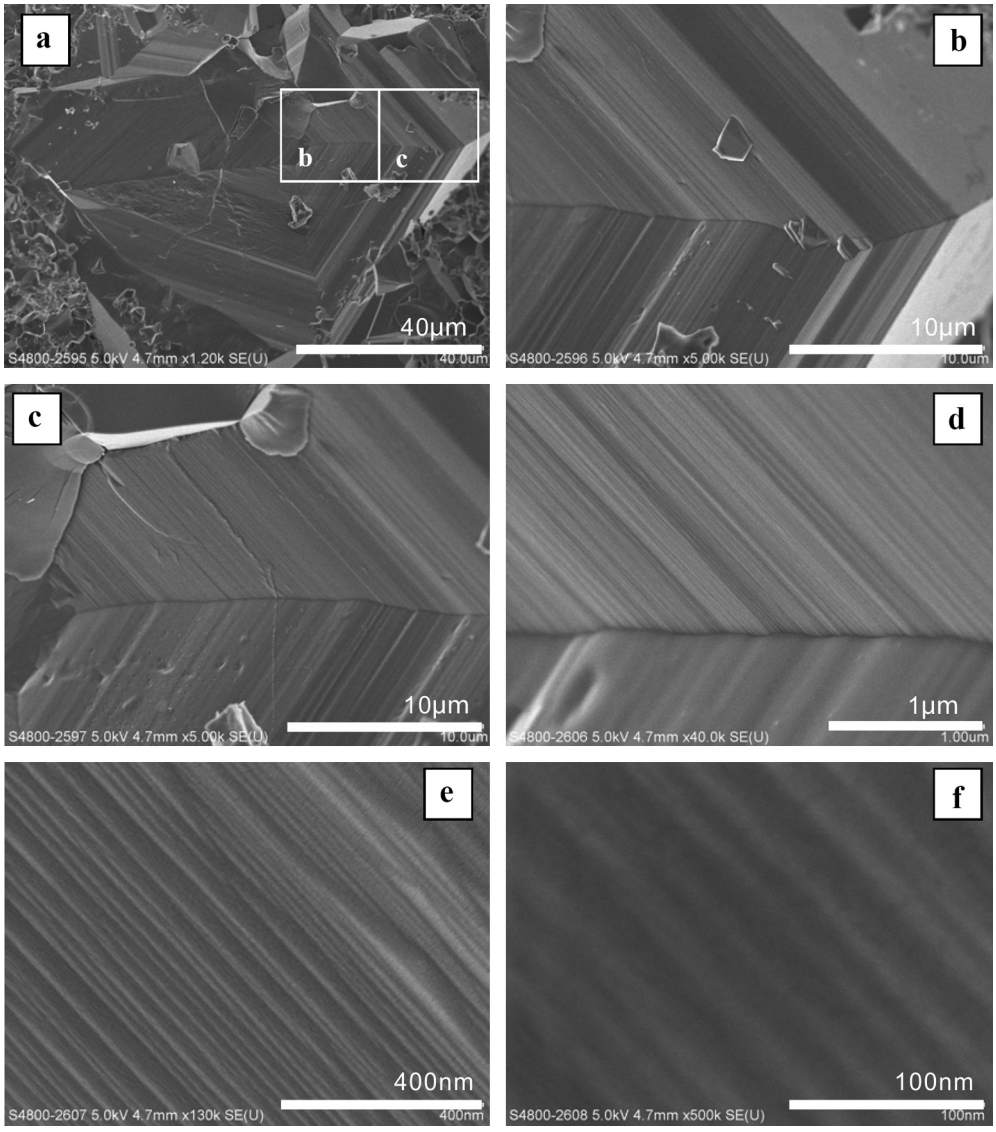

Fig. 9. The nanobands in the hematite blocks revealed by the falling-off of magnetite crystals. (a) shows a horizontal banding structure in a hematite pit after the falling-off of the magnetite. (b) and (c) amplify the areas marked "b" and "c" in (a). (d) and (e) provide step-by-step amplifications of (c) to reveal hematite nanobands.

Acknowledgements

I am thankful to Professor Axel Hofmann of the University of Johannesburg for providing the sample from the Kuruman Iron Formation. This study was supported by a General Research Fund (HKU7034129P) provided by the Hong Kong Research Grants Council.

References

Ahn, J.H., Buseck, P.R., 1990. Hematite nanospheres of possible colloidal origin from a Precambrian banded iron formation. Science 250, 111–113.
Anbar, A.D., Knoll, A.H., 2002. Proterozoic ocean chemistry and evolution: a bioinorganic bridge?. Science 297, 1137–1142.
Arbab, A.I., 2009. The length of the day: a cosmological perspective. Prog. Phys. 1, 8–11.
Barley, M.E., Pickard, A.D., Sylvester, P.J., 1997. Emplacement of a large igneous province as a possible cause of banded iron formation 2.45 billion years ago. Nature 385, 55–58.
Baur, M.E., Hayes, J.M., Studley, S.A., Walter, M.R., 1985. Millimeter-scale variations of stable isotope abundances in carbonates from banded iron-formations in the Hamersley Group of Western Australia. Econ. Geol. 80, 270–282.
Berman-Frank, I., Lundgren, P., Chen, Y.B., Küpper, H., Kolber, Z., Bergman, B., Falkowski, P., 2001. Segregation of nitrogen fixation and oxygenic photosynthesis in the marine cyanobacterium Trichodesmium. Science 294, 1534–1537.
Beukes, N.J., Gutzmer, J., 2008. Origin and paleoenvironmental significance of major iron formations at the Archean–Paleoproterozoic boundary. SEG Rev. 15, 5–47.
Bjerrum, C.J., Canfield, D.E., 2002. Ocean productivity before about 1.9 Gyr ago limited by phosphorus adsorption onto iron oxides. Nature 417, 159–162.
Braterman, P.S., Cairns-Smith, A.G., Sloper, R.W., 1983. Photo-oxidation of hydrated Fe^{2+}—Significance for banded iron formations. Nature 303, 163–164.
Brocks, J.J., Logan, G.A., Buick, R., Summons, R.E., 1999. Archean molecular fossils and the early rise of eukaryotes. Science 285, 1033–1036.
Castro, L.O., 1994. Genesis of banded iron-formations. Econ. Geol. 89, 1354–1397.
Chown, E.H., N'hah, E., Mueller, W.U., 2000. The relation between iron-formation and low temperature hydrothermal alternation in an Archean volcanic environment. Precambrian Res. 101, 263–275.
Cisne, J.L., 1984. A basin model for massive banded iron-formation and its geophysical applications. J. Geol. 5, 471–489.
Costas, E., González-Gil, S., López-Rodas, V., Aguilera, A., 1996. The influence of the slowing of Earth's rotation: a hypothesis to explain cell division synchrony under different day duration in earlier and later evolved unicellular algae. Helgol. Meeresunters. 50, 117–130.
Dukino, R.R., England, B.M., Kneeshaw, M., 2000. Phosphorus distribution in BIF-derived iron ores of Hamersley Province Western Australia. Appl. Earth Sci. 109, 168–176.
Dvornyk, V., Vinogradova, O., Nevo, E., 2003. Origin and evolution of circadian clock genes in prokaryotes. Proc. Natl. Acad. Sci. USA 100, 2495–2500.
Epping, E., Kühl, M., 2000. The responses of photosynthesis and oxygen consumption to short-term changes in temperature and irradiance in a cyanobacterial mat (Ebro Delta, Spain). Environ. Microbiol. 2, 465–474.

Eriksson, K.A., McCarthy, T.S., Truswell, J.F., 1975. Limestone formation and dolomitization in a lower Proterozoic succession from South Africa. J. Sediment. Res. 45, 604–614.
Ewers, W.E., Morris, R.E., 1981. Studies on the Dales Gorge Member of the Brockman Iron Formation, Western Australia. Econ. Geol. 76, 1929–1953.
Frei, R., Gaucher, C., Poulton, S.W., Canfield, D.E., 2009. Fluctuations in Precambrian atmospheric oxygenation recorded by chromium isotopes. Nature 461, 250–253.
Frost, C.D., von Blanckenburg, F., Schoenberg, R., Frost, B.R., Swapp, S.M., 2007. Preservation of Fe isotope heterogeneities during diagenesis and metamorphism of banded iron formation. Contrib. Mineral. Petrol. 153, 211–235.
Fru, E.C., Ivarsson, M., Kilias, S.P., Bengtson, S., Belivanova, V., Marone, F., Fortin, D., Broman, C., Stampanoni, M., 2013. Fossilized iron bacteria reveal a pathway to the biological origin of banded iron formation. Nat. Commun. 4, 2050. http://dx.doi.org/10.1038/ncomms3050.
Golden, S.S., Canales, S.R., 2003. Cyanobacterial circadian clocks—Timing is everything. Nat. Rev. Microbiol. 1, 191–199.
Hallberg, R., Ferris, F.G., 2004. Biomineralization by Gallionella. Geomicrobiol. J. 21, 325–330.
Hegler, F., Posth, N.R., Jiang, J., Kappler, A., 2008. Physiology of phototrophic iron(II)-oxidizing bacteria—implications for modern and ancient environments. FEMS Microbiology Ecology 66, 250–260.
Huberty, J.M., Konishi, H., Heck, P.R., Fournelle, J.H., Valley, J.W., Xu, H.F., 2012. Silician magnetite from the Dales Gorge Member of the Brockman iron formation, Hamersley Group, Western Australia. Am. Mineral. 97, 26–37.
Kappler, A., Pasquero, C., Konhauser, K.O., Newman, D.K., 2005. Deposition of banded iron formations by anoxygenic phototrophic Fe(II)-oxidizing bacteria. Geology 33, 865–868.
Kaufman, A.J., Hayes, J.M., Klein, C., 1990. Primary and diagenetic controls of isotopic compositions of iron-formation carbonate. Geochim. Cosmochim. Acta 54, 3461–3473.
Klein, C., 1973. Changes in mineral assemblages with metamorphism of some banded Precambrian iron-formations. Econ. Geol. 68, 1075–1088.
Klein, C., 2005. Some Precambrian banded iron-formations (BIFs) from around the world: their age, geological setting, mineralogy, metamorphism, geochemistry, and origin. Am. Mineral. 90, 1473–1499.
Kolo, K., Konhauser, K., Krumbein, W.E., van Ingelgem, Y., Hubin, A., Claeys, P., 2009. Microbial dissolution of hematite and associated cellular fossilization by reduced iron phases: a study of ancient microbe–mineral surface interactions. Astrobiology 9, 777–796.
Konhauser, K.O., Amskold, L., Lalonde, S.V., Postch, N.R., Kappler, A., Anbar, A., 2007. Decoupling photochemical Fe(II) oxidation from shallow-water BIF deposition. Earth Planet. Sci. Lett. 258, 87–100.
Konhauser, K., Hamada, T., Raiswell, R., Morris, R., Ferris, F., Southam, G., Canfield, D., 2002. Could bacteria have formed the Precambrian banded iron formations?. Geology 30, 1079–1082.
Konhauser, K.O., Lalonde, S.V., Planavsky, N.J., Pecoits, E., Lyons, T.W., Mojzsis, S.J., Rouxel, O.J., Barley, M.E., Rosiere, C., Fralick, P.W., Kump, L.R., Bekker, A., 2011. Aerobic bacterial pyrite oxidation and acid rock drainage during the Great Oxidation Event. Nature 478, 369–373.
Konhauser, K.O., Pecoits, E., Lalonde, S.V., Panineau, D., Nisbet, E.G., Barley, M.E., Arndt, N.T., Zahnle, K., Kamber, B.S., 2009. Oceanic nickel depletion and a methanogen famine before the Great Oxidation Event. Nature 458, 750–753.
Krapež, B., Barley, M.E., Pickard, A.L., 2003. Hydrothermal and resedimented origins of the precursor sediments to banded iron formation: sedimentological evidence from the early Palaeoproterozoic Brockman Supersequence of Western Australia. Sedimentology 50, 979–1011.
Kump, L.R., Barley, M.E., 2007. Increased subaerial volcanism and the rise of atmospheric oxygen 2.5 billion years ago. Nature 448, 1033–1036.
Li, Y.L., Konhauser, K.O., Cole, D.R., Phelps, T.J., 2011. Mineral ecophysiological data provide growing evidence for microbial activity in banded-iron formations. Geology 39, 707–710.
Li, Y.L., Cole, D.R., Konhauser, K., Chan, L.S., 2013a. Quartz nanocrystals in the 2.48-Ga Dales Gorge banded iron formation of Hamersley, Western Australia. Am. Mineral. 98, 582–587.
Li, Y.L., Konhauser, K.O., Kappler, A., Hao, X.L., 2013b. Experimental low-grade alteration of biogenic magnetite indicates microbial involvement in generation of banded iron formation. Earth Planet. Sci. Lett. 361, 229–237.
Li, Y.L., Sun, S., Chan, L.S., 2013c. Phosphogenesis in the 2460 and 2728 million-year-old banded iron formations as evidence for biological cycling of phosphate in the early biosphere. Ecol. Evol. 3, 115–125.
Liu, H., Wei, Y., Sun, Y., 2005. The formation of hematite from ferrihydrite using Fe(II) as a catalyst. J. Mol. Catal. A, Chem. 226, 135–140.
Marin-Carbonne, J., Rollion-Bard, C., Luais, B., 2011. In-situ measurements of iron isotopes by SIMS: MC-ICP-MS intercalibration and application to a magnetite crystal from the Gunflint chert. Chem. Geol. 285, 50–61.
Miyano, T., Beukes, N.J., 1984. Phase relations of stilpnomelane, ferriannite and riebeckite in very low-grade iron-formations. Trans. Geol. Soc. S.-Afr. 87, 111–124.
Morris, R.C., 1980. A textural and mineralogical study of the relationship of iron ore to banded iron-formation in the Hamersley iron province of Western Australia. Econ. Geol. 75, 184–209.
Morris, R.C., 1993. Genetic modeling for banded iron-formation of the Hamersley Group, Pilbara Carton, Western Australia. Precambrian Res. 60, 243–286.
Mueller, W.U., Mortensen, J.K., 2002. Age constrains and characteristics of subaqueous volcanic construction, the Archean Hunter Mine Group, Abitibi Greenstone belt. Precambrian Res. 115, 119–152.
Pecoits, E., Gingras, M.K., Barley, M.E., Kappler, A., Posth, N.R., Konhauser, K.O., 2009. Petrography and geochemistry of the Dales Gorge banded iron formation: paragenetic sequence, source and implications for palaeo-ocean chemistry. Precambrian Res. 172, 163–187.
Pickard, A.L., 2002. SHRIMP U–Pb zircon ages of tuffaceous mudrocks in the Brockman Iron Formation of the Hamersley Range, Western Australia. Aust. J. Earth Sci. 49, 491–507.
Pickard, A.L., 2003. SHRIMP U-Pb zircon ages for the Palaeoproterozoic Kuruman Iron Formation, Northern Cape Province, South Africa: evidence for simultaneous BIF deposition on Kaapvaal and Pilbara Cratons. Precambrian Res. 125, 275–315.
Posth, N.R., Hegler, F., Konhauser, K.O., Kappler, A., 2008. Alternating Si and Fe deposition caused by temperature fluctuations in Precambrian oceans. Nat. Geosci. 10, 703–708.
Posth, N.R., Konhauser, K.O., Kappler, A., 2013. Microbiological processes in banded iron formation deposition. Sedimentology 60, 1733–1754.
Poulton, S.W., Fralick, P.W., Canfield, D.E., 2004. The transition to a sulphidic ocean similar to 1.84 billion years ago. Nature 431, 173–177.
Rosso, K.M., Zachara, J.M., Fredrickson, J.K., Gorby, Y.A., Smith, S.C., 2003. Nonlocal bacterial electron transfer to hematite surfaces. Geochim. Cosmochim. Acta 67, 1081–1087.
Saito, M.A., Sigman, D.M., Morel, F.M.M., 2003. The bioinorganic chemistry of the ancient ocean: the co-evolution of cyanobacterial metal requirements and biogeochemical cycles at the Archean-Proterozoic boundary?. Inorg. Chim. Acta 356, 308–316.
Sergeev, V.N., Gerasimenko, L.M., Zavarzin, G.A., 2002. The Proterozoic history and present state of cyanobacteria. Microbiology 71, 623–637.
Stal, L.J., Krumbein, W.E., 1986. Metabolism of cyanobacteria in anaerobic marine sediments. Actes Colloq. IFREMER 3, 301–309.
Steinhoefel, G., Horn, I., von Blanckenburg, F., 2009. Micro-scale tracing of Fe and Si isotope signatures in banded iron formation using femtosecond laser ablation. Geochim. Cosmochim. Acta 73, 5343–5360.
Steinhoefel, G., von Blanckenburg, F., Horn, I., Konhauser, K.O., Beukes, N.J., Gutzmer, J., 2010. Deciphering formation processes of banded iron formations from the Transvaal and the Hamersley successions by combined Si and Fe isotope analysis using UV femtosecond laser ablation. Geochim. Cosmochim. Acta 74, 2677–2696.
Trendall, A., 2000. The significance of banded iron formation (BIF) in the Precambrian stratigraphic record. Geoscientist 10, 4–7.
Trendall, A.F., 2002. The significance of iron-formation in the Precambrian stratigraphic record. In: Altermann, W., Corcoran, P.L. (Eds.), Precambrian Sedimentary Environments: A Modern Approach to Ancient Depositional Systems, Special Publication No. 33 of the International Association of Sedimentologists. Blackwell Science, pp. 33–66.
Trendall, A.F., Blockley, J.G., 1970. The iron formation of the Precambrian Hamersley Group, Western Australia. Bull. - Geol. Surv. West. Aust. 119.
Trendall, A.F., Compston, W., Nelson, D.R., De Laeter, J.R., Bennett, V.C., 2004. SHIMP zircon ages constraining the depositional chronology of the Hamersley Group, Western Australia. Aust. J. Earth Sci. 51, 621–644.
Walker, J.C.G., Zahnle, K.J., 1986. Lunar nodal tide and distance to the Moon during the Precambrian. Nature 320, 600–602.
Walter, M.R., Hofmann, A.F., 1983. The palaeontology and palaeoecology of Precambrian iron-formations. In: Trendall, A.F., Morris, R.C. (Eds.), Iron-Formation Facts and Problems, Developments in Precambrian Geology, vol. 6. Elsevier, pp. 373–400.
Wang, Y., Xu, H., Merino, E., Konishi, H., 2009. Generation of banded iron formations by internal dynamics and leaching of ocean crust. Nat. Geosci. 2, 781–784.
Weiershäuser, L., Spooner, E.T.C., 2005. Seafloor hydrothermal fluids, Ben Nevis area, Abitibi Greenstone Belt: implications for Archean (~2.7 Ga) seawater properties. Precambrian Res. 138, 89–123.
Williams, G.E., 2000. Geological constrains on the Precambrian history of Earth's rotation and the Moon's orbit. Rev. Geophys. 38, 37–59.